Characterizing Molecular Gas Towards Sagittarius B2: The Galactic Center's Complex Giant Molecular Cloud

V. Donofrio,[1] J. Ott,[2] D. Meier,[2,3] and B. Svoboda[2]

[1]*Michigan State University, East Lansing, MI*
[2]*National Radio Astronomy Observatory, Socorro, NM*
[3]*New Mexico Institute of Mining and Technology, Socorro, NM*

ABSTRACT

We present ~ 0.9 pc resolution ATCA observations toward twelve protostellar core regions in Sagittarius B2 (Sgr B2). We detected 28 of a possible 42 spectral features to be present in emission and absorption components in these regions throughout the cloud, including but not limited to: metastable and non-metastable ammonia inversion lines, complex organic molecules (COMs), and shock tracers. We aimed to study the general physical strucutre of Sgr B2. We found that the typical velocity range in the cloud is ~ 55 km s^{-1} $-$ ~ 70 km s^{-1} with velocities as high as ~ 120 km s^{-1}. We also found that many regions possess large velocity widths (≥ 35 km s^{-1}), indicating that the cloud is participating in mass motions such as expansion. We found evidence in the temperature distribution of the cloud that the general structure of Sgr B2 contains hot, dense molecular cores in the central regions with cooler outskirts. We were able to illustrate that Region N, Region M, and Region U all possess star forming characteristics, significantly more so than the other regions.

1. INTRODUCTION

Sagittarius B2 (Sgr B2) is a giant molecular cloud (GMC) located near the center of the Milky Way Galaxy in a chemically rich region known as the Central Molecular Zone (CMZ). The CMZ represents the inner 500 pc of the Galactic Center (GC) and is comprised of a plethora of GMCs that have highly active star formation. With an abundance of dense, molecular gas, the CMZ has a star formation rate (SFR) between 0.1 M$_\odot$ yr^{-1} and 0.8 M$_\odot$ yr^{-1} (Longmore et al. 2013a; Lada et al. 2012) which makes up much of the total star forming activity in the entire 30 kpc of the Milky Way, that itself produces upwards of 2 M$_\odot$ yr^{-1} (Licquia & Newman 2015).

Deep in the center of the CMZ is the supermassive black hole Sagittarius A* which the many molecular clouds in the CMZ orbit around. The immediate region around Sgr A* is not an active star forming site; however, the molecular clouds that orbit are. Specifically, as the distance of the cloud from the supermassive black hole increases, so does the SFR (Longmore et al. 2013b).

Approximately 100 pc from Sgr A* lies Sgr B2, which is the largest cloud near the GC with a size of 40 pc and total mass of 10^7 M$_\odot$ (Goldsmith et al. 1990); the inner 20 pc of the cloud contains approximately 99 percent of the total mass (Lis & Goldsmith 1989). Towards the center of Sgr B2 lie two well-known regions: North (N) and Main (M). These two regions are dense, hot molecular cores that comprise much of the known star forming activity in Sgr B2; between these two regions are 70 high mass stars (Pree et al. 1998).

In this report, we present the characterization of the molecular gas towards twelve protostellar core regions located in Sgr B2. This allows us to characterize physical conditions throughout Sgr B2. Specifically, we focus on the lesser-known regions around Sgr B2 (those not N and M). While we still include N and M in the analysis, a unique aspect of this project is the simultaneous comparison of multiple regions throughout the giant molecular cloud which is attributable to the nature of the survey used.

2. OBSERVATIONS AND DATA

2.1. *Observations*

The "Survey of Water and Ammonia in the Galactic Center" (SWAG) is a survey intended to map the molecular content of the entire Central Molecular Zone (CMZ) of the Milky Way Galaxy. The observations were obtained using the Australia Telescope Compact Array (ATCA), an array of six 22-m antennas a part of the

Paul Wild Observatory in Narrabri, New South Wales, Australia. The survey maps the CMZ from a Galactic longitude of $\sim -1°$ to $\sim +2°$ at Galactic latitudes $|b| < 0.4°$. The spatial resolution is ~ 22.8" with a range of $20.6" - 25.0$" for the frequency range of 21.2 GHz $- 25.4$ GHz; this corresponds to ~ 0.9 pc. The velocity resolution is ~ 0.4 km s^{-1} with a range of 0.37 km s$^{-1} - 0.45$ km s^{-1}. Using the ATCA, observations were performed using ~ 6500 individual pointings with integration times of ~ 4 minutes per pointing. In total, the observations required ~ 525 hours spanned over three years (2014 - 2016).

The observations targeted 42 spectral lines at a wavelength of 1.3 cm, including ammonia metastable and non-metastable inversion lines, complex organic molecules, and radio recombination lines. At least 20 of these spectral features are explicitly identified (Krieger et al. 2017).

2.2. *Spectral Line Identification*

To make use of the physical implications the gas of a molecule indicates, we need to make sure that the targeted spectral line is determined unambiguously. From the targeted 42 spectral lines in the SWAG data set, we determined 14 to be removed from further consideration.

To be considered unambiguously identified, the examined spectral profiles of the spectral line could not appear to be contaminated by another line, be a duplicate of another line, or have no detectable components. These lines that were eliminated from consideration, including reason for removal, as well as the remaining lines are summarized in Table 4 in Appendix.

2.3. *Sagittarius B2 Regions*

Twelve regions in Sagittarius B2 (Sgr B2) were chosen for analysis. Many of these correspond to prominent molecular cores and H II regions throughout the cloud. Considering that 99 percent of the mass in Sgr B2 resides in its inner 20 pc, all of these regions are located in this range. Additionally, these twelve regions correspond to bright radio continuum sources that appear in the cloud. Figure 1 illustrates these regions while Table 1 summarizes the positions.

As previously mentioned, North (N) and Main (M) are the two most well-studied regions in Sgr B2, each being large, dense molecular cores. Regions L, R, U, and V all possess a shell-like structure. Region R shows edge brightening in its east and west positions. Region U appears either as an edge brightened or cometary region. Region V appears shell-like with a clumpy intensity distribution. Region AA is associated with diffuse emission. Region BB appears to be an edge brightened H II

region (Mehringer et al. 1993). Region Deep South (DS) is a long molecular dust ridge (Ginsburg et al. 2018). Region South (S) is one of the more well-studied regions and is a dense molecular core similar to N and M; however, it is not as large (Mehringer et al. 1993).

The two southern most regions are not literature identified sources and are given the identifications SE (South Extra) and SE2 (South Extra Two) for this project. The previous ten regions use identifications that are commonly accepted in the literature (Mehringer et al. 1993). The observational parameters in Table 1 corresponds to the position of peak brightness temperature (K) in the region with a beam size of 30"x30".
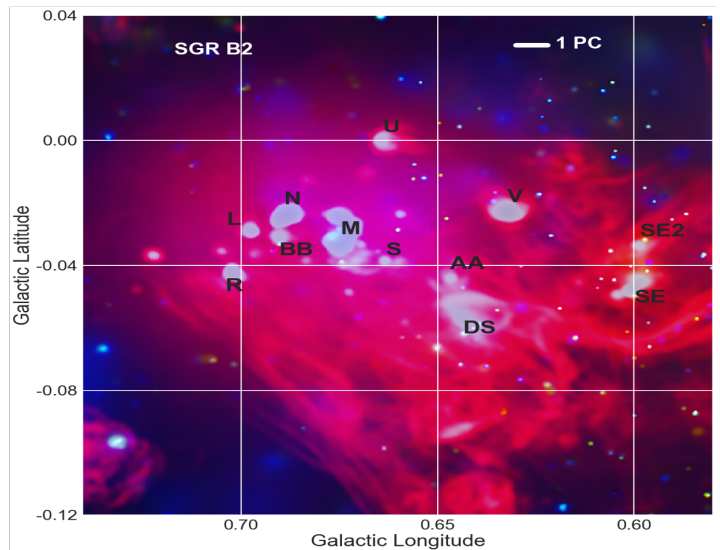

Figure 1. Figure of the twelve Sgr B2 regions analyzed in this report. This plot captures the inner 20 pc of the cloud which contains majority of its mass. Each region corresponds to a bright radio continuum source. The image is an x-ray and radio composite with data from the Chandra x-ray telescope (green and blue) combined with radio data (red) from the MeerKAT radio telescope (Wang et al. 2019).

3. RESULTS

3.1. *Spectral Profiles*

Using the observational parameters in Table 1, we extracted spectral profiles of each region for each spectral line. Since we will be comparing lines, we smooth each data cube to a common beam size of 30"x30" using CASA. The spectral profile for a given region in a data cube is selected with a point region at the corresponding location in Table 1.

To compare each spectral line and examine physical conditions of Sgr B2, we need to define a reference line. The spectral line best suited to serve as a reference is NH$_3$(3,3) with rest frequency 23.87 GHz; it is noted as

Table 1. Observational Parameters of Regions in Sgr B2.

Region	Peak Position		
	α(J2000)	δ(J2000)	Brightness Temperature of Radio Continuum (K)
Sgr B2 AA	$17^h47^m50^s.36$	$-28°22'60"$	18.44
BB	17 47 53.02	-28 20 36	5.77
DS	17 47 52.19	-28 23 23	2.94
L	17 47 53.82	-28 20 16	4.52
M	17 47 50.97	-28 21 25	27.84
N	17 47 50.91	-28 20 35	15.35
R	17 47 57.13	-28 20 24	3.37
S	17 47 51.22	-28 22 06	3.73
SE	17 47 45.21	-28 25 11	3.91
SE2	17 47 42.17	-28 24 53	1.13
U	17 47 42.98	-28 20 57	1.23
V	17 47 44.04	-28 23 03	3.40

the most established column density tracer in Sgr B2 compared to the other lines in the data set. For each region's spectral profile for NH$_3$(3,3), we Gaussian fit the emission or absorption component that corresponds to a Sgr B2 velocity ($0-120$ km s^{-1}) to find the velocity centroid. Once these velocity centroid values were found for the spectra of the reference line, the brightness temperatures that correspond to the velocity component for each other line was found. To ensure that the absorption or emission component for a given cube is meaningful, we require that the brightness value must be greater than three times the RMS (σ) (σ values found in Table 4 in Appendix) of the data cube ($T_{measured} > 3\sigma$). About one-third of the corresponding velocity components totaled from each data cube are less than the 3σ value. Additionally, single-channel components were considered an artifact of the spectral profile.

The spectral profile for Region L in NH$_3$(3,3) can be used to exemplify this process which is shown in Figure 2. Fitting the velocity range between ~ 25 km s^{-1} to ~ 125 km s^{-1} gave a velocity centroid for the bright emission component of 69.11 km s^{-1}. For the L region spectral profiles for each remaining cube, we determine if the emission or absorption component that corresponds to this velocity is greater than 3σ; if it is, we consider that component to calculate the line ratio of each spectral line. It is important to note that while most Sgr B2 regions for the reference line NH$_3$(3,3) contained a meaningful velocity component, Region U did not. To counteract this, we substituted the velocity component of Region U with that of NH$_3$(1,1) with rest frequency 23.69 GHz as this was a meaningful component.

As some of the components we consider are in absorption, we need to convert from brightness temperature to opacity. This can be done using

$$\tau = -\ln(1 - \frac{|T_L|}{T_C}), \qquad (1)$$

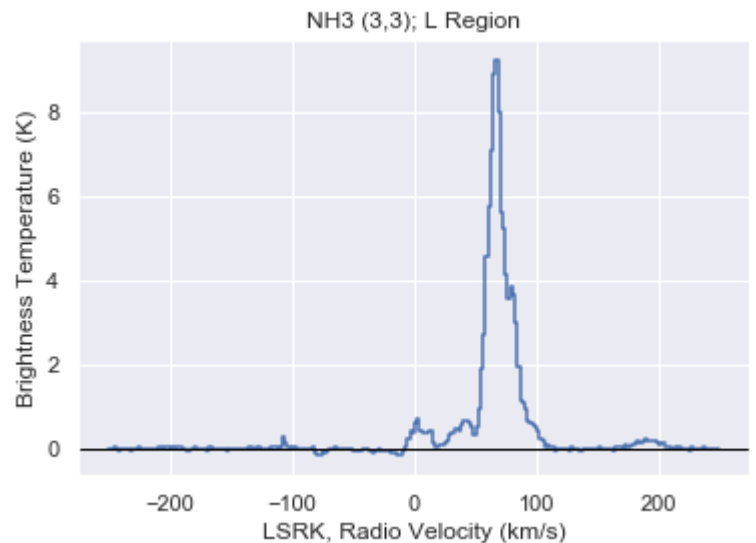where $T_L = T_{measured} - T_C$ and T_C is the brightness temperature of the continuum which is found in Table 1.

NH3 (3,3); L Region

Figure 2. This plot features the spectral profile of Region L in NH$_3$(3,3). The y-axis is brightness temperature of the source in K while the x-axis is velocity in km s^{-1} (LSRK). By fitting the emission component in this profile with a single Gaussian component, the velocity centroid, FWHM, and peak brightness values can be found. In this case, the values are 69.11 km s^{-1}, 20.28 km s^{-1}, and 7.76 K.

3.2. *Physical Structure: Velocities, Velocity Widths, and Integrated Profiles*

We next use the reference line of $NH_3(3,3)$ ($NH_3(1,1)$ for Region U) to characterize physical conditions of Sgr
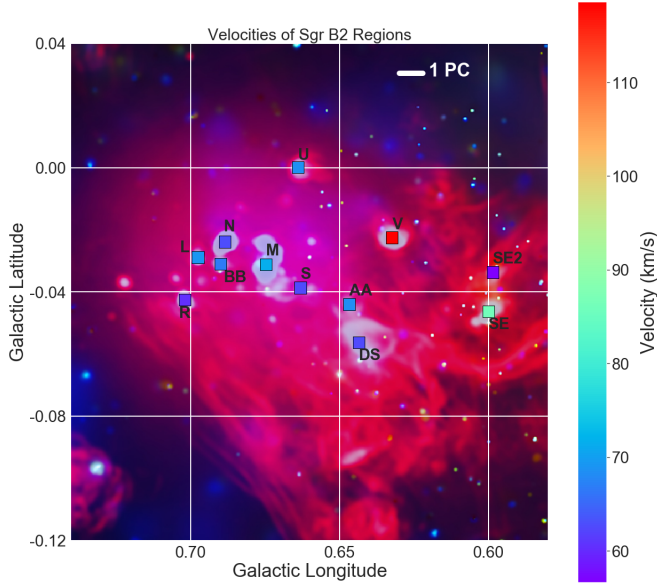

Figure 3. This figure shows the velocity values of the twelve Sgr B2 regions in km s^{-1} by color scale, with higher velocities redder in color and lower velocities bluer. The values are fairly uniform throughout the cloud with a range of ~ 55 km s^{-1} $- \sim 70$ km s^{-1}. The outstanding region is Region V with a velocity of 118.63 km s^{-1}. Background image credit: (Wang et al. 2019).

B2; specifically in velocity (km s^{-1}), velocity width (km s^{-1}), and integrated profile (K km s^{-1}) values. The velocity values correspond to the velocity centroid values of the Sgr B2 component for each region. The velocity width values correspond to the FWHM value of the Gaussan fit component. The integrated profile values are found using

$$F_{line} = 1.065(T_{measured})\Delta V, \qquad (2)$$

where ΔV is the FWHM of the velocity component. The velocities, velocity widths, and integrated profiles are illustrated in Figure 3, Figure 4, and Figure 5, respectively. A summary of the physical parameters are found in Table 2. Looking at Figure 3, the velocities of the regions in Sgr B2 are fairly uniform throughout the cloud, with values typically appearing in the range of ~ 55 km s^{-1} $- \sim 70$ km s^{-1}. An interesting region to note is Region V, which has a Sgr B2 velocity component of 118.63 km s^{-1} and is much higher than the rest of the regions. Figure 4 shows that the velocity widths of the regions in Sgr B2 are large towards the center of
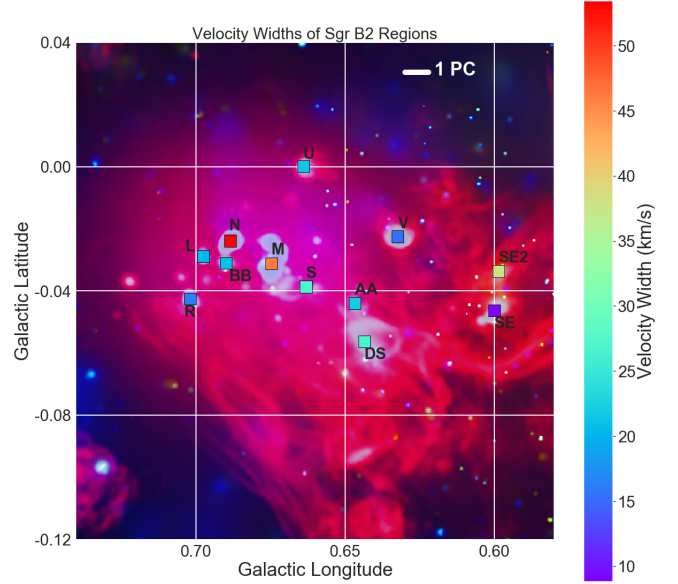

Figure 4. This figure shows the velocity width values of the twelve Sgr B2 regions in km s^{-1} by color scale. The values are larger towards the center of the cloud and tend to narrow towards the outskirts. Many regions possess a relatively large velocity width value of ≥ 35 km s^{-1}. Background image credit: (Wang et al. 2019).
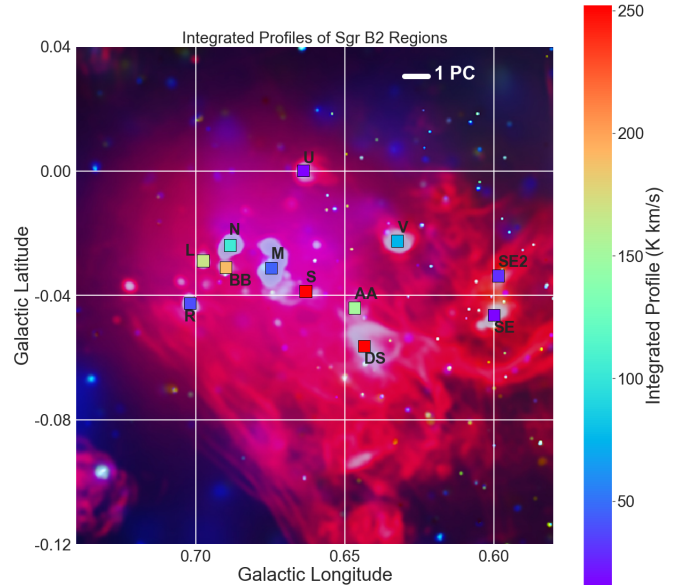

Figure 5. This figure shows the integrated profile values of the twelve Sgr B2 regions in km s^{-1} by color scale. The values tend to be larger towards the center of the cloud and tend to narrow towards the outskirts, indicating a warmer central area of the cloud. Background image credit: (Wang et al. 2019).

the cloud, and narrow as the regions reach the outskirts. The larger velocity widths hint at the idea that these regions are broader, more turbulent, and larger clumps of

material. From Figure 4, we would see that regions N and M contain extremely wide velocity widths, with a gradual decrease towards the outskirts; Region SE2 is an exception that possesses a relatively high width. This result suggests that the center of Sgr B2 is made up of dense, clumpy, and expanding material.

Figure 5 shows less consistent results when regarding the integrated profile of each region. We do see however, that the stretch of regions from the furthest north region (Region L) to Region DS generally possess the higher integrated profile values. The regions on the western edge of Sgr B2 (regions U, V, SE, SE2) all possess relatively low values; the eastern most region (Region R) also shares this characteristic. The integrated profile of a region incorporates the velocity width and peak brightness temperature for the Sgr B2 velocity component of that region; so, a higher value is likely to possess a hotter temperature and a large velocity width. This suggests that for the strip of regions with a relatively high integrated profile, they are warmer and clumpier regions than those on the western and eastern outskirts of the cloud.

Overall, these physical parameters indicate that the general structure of Sgr B2 consists of gas moving approximately in the range ~ 55 km s^{-1} $-$ ~ 70 km s^{-1} with a distribution of dense, hot molecular cores towards it center and small, cool regions toward its outskirts.

3.3. Calculating Line Ratios

To make various comparisons between the remaining spectral features in the data set, we can construct line ratios. As briefly mentioned in Section 3.1, the line ratio for a Sgr B2 region for a certain spectral line is found by calculating the ratio of brightness temperature for that region to the brightness temperature of the reference line (NH_3(3,3) for all except Region U where NH_3(1,1) is the reference). The brightness temperature corresponds to the emission or absorption component of the velocity component determined by the reference line. This ensures that each emission or absorption component we are analyzing corresponds to a meaningful Sgr B2 component.

Figure 11 in Appendix comprises the line ratios for each Sgr B2 region of each spectral line. The ratios colored in red correspond to emission components and the ratios colored in blue correspond to absorption components. Those panels that feature no ratio for a given region are due to a meaningless emission or absorption component; the brightness temperature was less than the 3σ value discussed in Section 3.1 and so did not correspond to Sgr B2, but instead corresponds to the noise

in the spectral profile. The σ values are found in Table 4 in Appendix.

We can use the common comparison of each spectral line to a reference to find rotational temperature values of the regions in Sgr B2 as well as characterize the molecular gas in the cloud to illustrate star formation features. We will use 14 spectral lines comprising of metastable ammonia inversion lines, non-metastable ammonia inversion lines, complex organic molecules, and shock tracers to accomplish this; the former will be used in the rotational temperature caluclation while the latter three will be used to illustrate star forming tracers.

3.4. Rotational Temperature using Ammonia Metastable Inversion Lines

Using line ratios of inversion lines of metastable ammonia, where rotational quantum numbers J and K are equal ($J = K$), we can calculate the rotational temperature (T_{rot}) of the regions in Sgr B2. Considering that for the metstable inversion lines, radiative decay is especially slow, T_{rot} is to first order similar to the kinetic temperature (T_{kin}) of the dense, molecular gas of a molecular cloud (Walmsley & Ungerechts 1983).

When considering emission, multiple metastable inversion doublets need to be determined. In this case, we make use of NH_3(2,2) with rest frequency 23.72 GHz and NH_3(4,4) with rest frequency 24.14 GHz. In optically thin emission, the column densities of their upper states are found using

$$N_u(J,K) = \frac{7.77 \cdot 10^{13}}{\nu} \frac{J(J+1)}{K^2} \int T_{mb} \, dv \qquad (3)$$

where J and K are the quantum numbers, ν is the frequency, T_{mb} is the main beam brightness temperature, and v is the velocity (Henkel et al. 2000). In absorption, the excitation temperature T_{ex} across an inversion doublet allows us to use

$$\frac{N_u(J,K)}{T_{ex}} = 1.61 \cdot 10^{14} \frac{J(J+1)}{K^2 \nu} \tau \Delta v_{1/2}, \qquad (4)$$

where $\Delta v_{1/2}$ is the FWHM of the line and τ is found using equation 1 (Hüttemeister et al. 1995). We assume for each transition T_{ex} is the same, so it cancels. Using a pair of ammonia metastable inversion lines, the rotational temperature $T_{JJ'}$ can be found using

$$\frac{N_u(J',J')}{N_u(J,J)} = \frac{2J'+1}{2J+1} \exp(\frac{-\Delta E}{T_{JJ'}}), \qquad (5)$$

where J' and J are the quantum numbers of the respective inversion lines and ΔE is the energy difference between them (Henkel et al. 2000). The line ratios are

Table 2. Summary of Physical Parameters of Regions in Sgr B2.

Region	Velocity (km s^{-1})	Velocity Width (km s^{-1})	Integrated Profile (K km s^{-1})
Sgr B2 AA	68.37	22.03	151.56
BB	66.65	21.05	190.11
DS	62.66	26.69	252.41
L	69.11	20.28	167.60
M	71.47	46.19	45.75
N	62.90	53.47	103.64
R	60.32	16.32	38.59
S	62.66	26.69	252.41
SE	86.10	8.85	16.49
SE2	56.65	38.12	29.23
U	68.61	21.41	15.28
V	118.63	15.35	74.71

substituted into the parameter of their respective absorption or emission equation, and the calculated N_u value is substituted into eq. 5. This simplifies into the following for $T_{JJ'}$

$$T_{JJ'} = \frac{-\Delta E}{\ln(0.455 \frac{T_{J,J}}{T_{J',J'}})}, \tag{6}$$

where $J = 4$, $J' = 2$, the energy difference $\Delta E = 136$ K, $T_{J,J}$ is the brightness temperature for $NH_3(4,4)$, and $T_{J',J'}$ is the brightness temperature for $NH_3(2,2)$ (Walmsley & Ungerechts 1983). Figure 6 illustrates $T_{JJ'}$ for each Sgr B2 region while Table 3 summarizes the values. We observe similar results to Section 3.2 where the central regions possess relatively warmer temperatures than those on the outskirts of the cloud. Particularly, the rotational temperature illustration follows extremely similarly to the integrated profile results in Figure 5. We see that starting from the northern most region (Region L) down to Region DS the temperatures are generally warmer than those on the western outskirts (V, SE, SE2) and the eastern outskirts (R) of the cloud. Additionally, we witness in both of those plots that Region M is unexpectedly colder than the rest of the central regions, with an integrated profile of 45.75 K km s^{-1} and rotational temperature of 78.05 K. This is likely due to the fact that our observation towards Region M is not actually observing M proper, but instead absorption along the line-of-site of Region M. For the two ammonia metastable inversion lines used to calculate the rotational temperature, Region M contains an absorption component, meaning it is reasonable to expect a cooler temperature. As a result, the observation towards Region M in our data set could simply be picking up the molecular gas of the outskirts of the cloud along the line-of-sight of Region M, making the region possess low temperature values.

Another region to note is Region U. Considering the rotational temperature between two inversion lines can only be found when the lines are in both emission or absorption, we cannot calculate a value for U. For $NH_3(4,4)$, Region U is found in absorption while for $NH_3(2,2)$, Region U is found in emission. This suggests interesting non-LTE behavior in NH_3 towards Region U.

Overall, the temperature distribution of the cloud is fairly narrow with a range of ~ 60 K $- \sim 160$ K.

Table 3. Summary of Rotational Temperatures for Regions in Sgr B2.

Region	Rotational Temperature $T_{JJ'}$ (K)
Sgr B2 AA	105.61
BB	110.45
DS	124.98
L	97.496
M	78.053
N	167.37
R	85.228
S	124.98
SE	83.522
SE2	62.499
U	
V	90.799

3.5. Line Ratios for Non-metastable Ammonia Inversion Lines

Non-metstable inversion lines of ammonia can be used to characterize star forming features of molecular clouds. In the presence of background infrared radiation, the rapid decay of non-metastable states into metastable states allows for the tracing of the radiation environ-
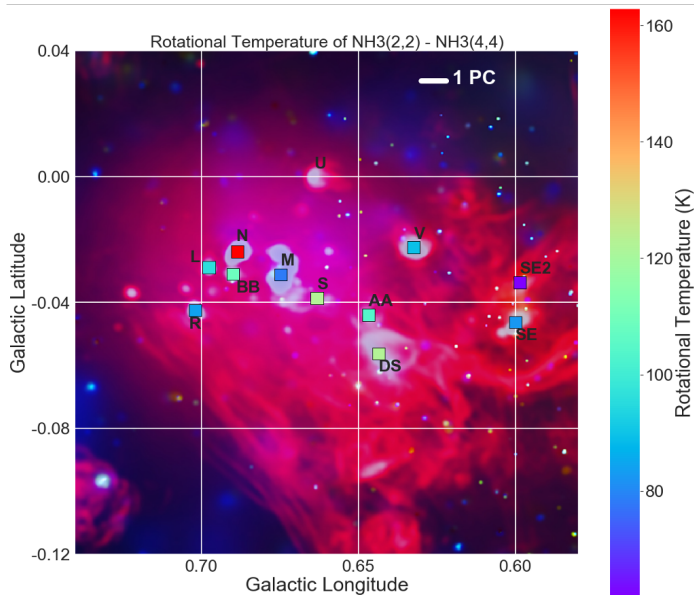
Figure 6. This figure shows the rotational temperature values of the twelve Sgr B2 regions in km s^{-1} by color scale. The two metastable ammonia inversion lines used to find these values are NH$_3$(2,2) with rest frequency 23.72 GHz and NH$_3$(4,4) with rest frequency 24.14 GHz. As is the trend in Figure 5, the central regions tend to be warmer than the outskirts. The range of the values are $\sim$ 60 K $- \sim$ 160 K. Region M is observed in absorption for these inversion lines indicating we are picking up outskirts along its line-of-sight, lowering the temperature. Region U is observed in emission for NH$_3$(2,2) and absorption for NH$_3$(4,4), so the rotational temperature cannot be found. Background image credit: (Wang et al. 2019).

ment within star forming regions. The ammonia non-metastable inversion lines we analyze are NH$_3$(2,1) with rest frequency 23.10 GHz, NH$_3$(3,2) with rest frequency 22.83 GHz, and NH$_3$(4,3) with rest frequency 22.69 GHz.

Figure 7 shows the line ratios of each Sgr B2 region for these three spectral lines. We find that Region N and Region M dominate the other regions, which we expect due to their noted star forming activity. However, we also find that Region U is consistently present and dominates the remaining regions, indicating possible features of star formation. It is important to note here the extremely high emission components for Region M. In Section 3.2 and Section 3.4 we found Region M to be unexpectedly cool, likely due to the fact that we are not observing M proper. These high emission components hint at the idea that M proper should be fairly warm, supporting the previous notion that we are observing along the line-of-sight of Region M and factoring in cooler outskirts of Sgr B2.

3.6. Line Ratios for Shock Tracers and Complex Organic Molecules

Both shock tracing and complex organic molecules (COMs) are abundant on ice grain surfaces within molecular clouds. During cloud-cloud collisions or nearby supernovae, these molecules are liberated into the gaseous phase, therefore allowing these molecules to trace shocks. Likewise, these shock-inducing events are known to trigger star formation in molecular clouds (Zeng et al. 2020). The shock tracing molecules analyzed are HNCO ($1_{0,1} - 0_{0,0}$, $F = 2 - 1$) with rest frequency 21.98 GHz and CH$_3$OH ($3_{1,2} - 3_{0,3}$) with rest frequency 24.93 GHz. The complex organic molecules are CH$_3$OCHO ($2_{1,2} - 1_{1,1}$) with rest frequency 22.83 GHz, HCOOH ($1_{0,1} - 0_{0,0}$) with rest frequency 22.47 GHz, and NH$_2$CHO ($1_{0,1} - 0_{0,0}$, $F = 2 - 1$) with rest frequency 21.21 GHz.

Figure 8 shows the line ratios of each Sgr B2 region for these spectral lines. We find that Region N and Region M dominate the other regions, as expected. We again find that Region U is consistently present and dominates the remaining regions, indicating possible features of star formation. It is important to note for the shock tracers that the high emission in Region N and Region M is likely due to evaporation instead of recently shocked gas because of the known extremely hot temperatures exhibited in these regions. The remaining sources are cool enough to likely feature recently shocked material, like in Region U.

4. DISCUSSION

Our results have allowed us to characterize the general physical make-up of Sgr B2 as well as hint at star forming features that abundantly comprise select regions in the cloud.

4.1. Physical Conditions and Structure of Sgr B2

Our results for rotational temperature (Figure 6 and Table 3) and integrated profile (Figure 5 and Table 2 have indicated that the general structure of Sgr B2 is comprised of clumpy, hot regions towards the central areas of the cloud, while the outskirts are cooler and less dense. Additionally, it is important to note that our results indicate that there is a gradually descent in temperature as the distance increases from the center of the cloud. This agrees with the temperature distribution in Mehringer et al. (1993).

We also find in Figure 3 and Table 2 that the velocity range of the molecular gas in most regions exists in a range of $\sim$ 55 km s^{-1} $- \sim$ 70 km s^{-1} which agrees with Mehringer et al. (1993) results that found that most of the gas throughout Sgr B2 was in the range $\sim$ 50 km s^{-1}
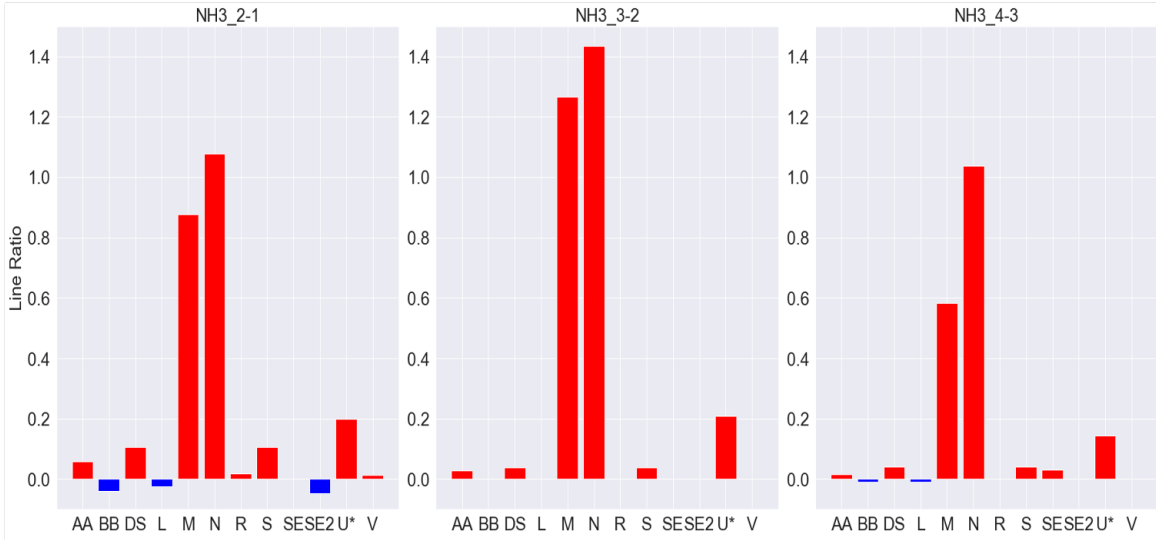
Figure 7. This figure shows the line ratios for three non-metastable ammonia inversion lines: $NH_3(2,1)$ with rest frequency 23.10 GHz, $NH_3(3,2)$ with rest frequency 22.83 GHz, and $NH_3(4,3)$ with rest frequency 22.69 GHz. The red bars represent emission components and the blue bars represent absorption components. Region N and Region M are dominate, but Region U is consistently present, as well.
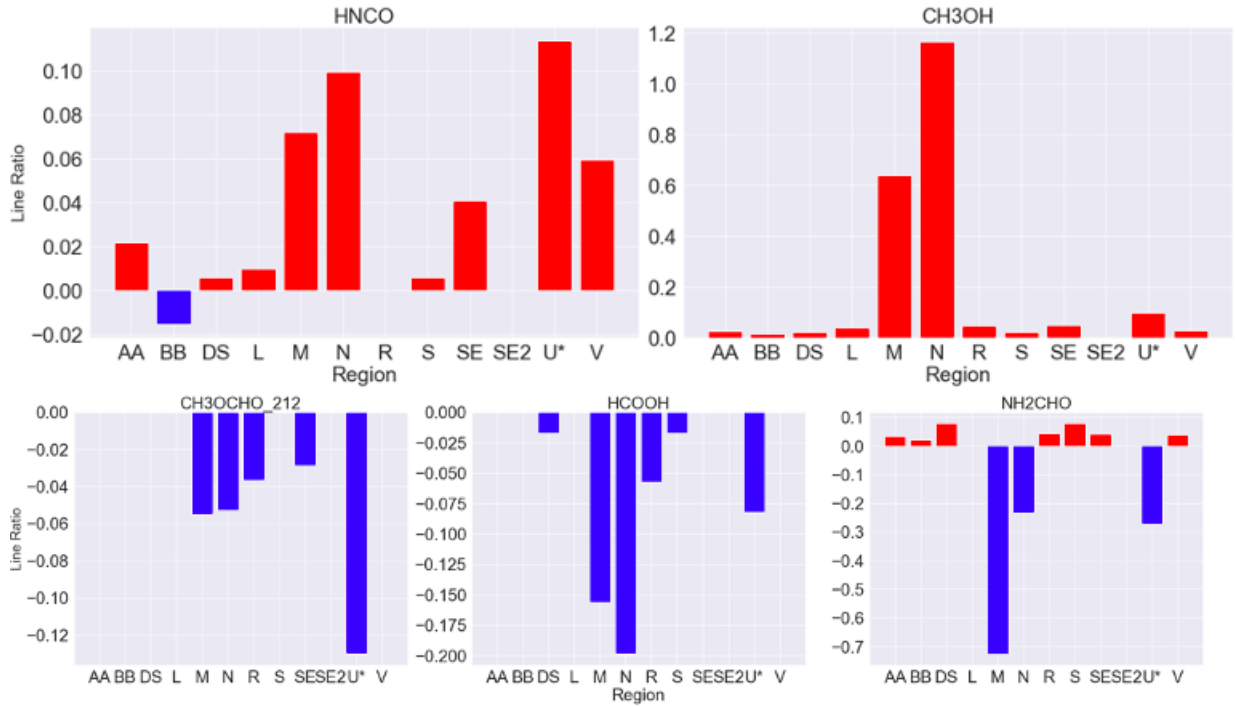

Figure 8. This figure shows the line ratios for the shock tracers and COMs as follows: HNCO ($1_{0,1} - 0_{0,0}$, $F = 2 - 1$) with rest frequency 21.98 GHz, CH_3OH ($3_{1,2} - 3_{0,3}$) with rest frequency 24.93 GHz, CH_3OCHO ($2_{1,2} - 1_{1,1}$) with rest frequency 22.83 GHz, HCOOH ($1_{0,1} - 0_{0,0}$) with rest frequency 22.47 GHz, and NH_2CHO ($1_{0,1} - 0_{0,0}$, $F = 2 - 1$) with rest frequency 21.21 GHz. The red bars represent emission components and the blue bars represent absorption components. Region N and Region M are dominate, but Region U is consistently present, as well. Region N and Region M are likely to be bright in emission due to evaporation, not recent shocks.

$- \sim 70$ km s^{-1}. Additionally, we found that the velocity for Region V of 118.63 km s^{-1} was extremely outstanding. However, this approximately agrees with the find-ing in Mehringer et al. (1993) for Region V where the velocity component was ~ 100 km s^{-1} and likewise outstanding to the other regions. Furthermore, Mehringer

et al. (1993) finds many regions in Sgr B2 to possess a velocity width ≥ 40 km s^{-1}, indicating that the gas could be expanding, or participating in mass motions. Our results in Figure 4 and Table 2 find many regions to possess a velocity width of approximately the same nature (≥ 35 km s^{-1}), particularly towards the center of the cloud.

4.2. *Sgr B2 Regions Exhibiting Star Forming Characteristics*

The results in Section 3.5 and Section 3.6 found that there are three Sgr B2 regions that are chemically rich in star forming tracers such as non-metastable ammonia inversion lines and shock tracers; these regions are Region N, Region M, and Region U. Ginsburg et al. (2018) states that highly active star forming is not just occurring in the famous N and M regions, but over an extended region spanning much of the Sgr B2 cloud indicated by a plethora of high-mass protostellar cores.

The three regions we found in this report to richly feature star forming characteristics can be illustrated by the model in Hasegawa et al. (1994) which is featured in Figure 9. Looking at Figure 9, this model suggests that the very dense Clump collided with a less dense molecular cloud that resulted in the removal of gas and the Hole in it. This cloud-cloud collision would shock the nearby gas in the overall cloud of Sgr B2 and trigger a scenario of starbursts.

The relation to our results can be illustrated with Figure 10. The blue ring in the figure highlighting the northwestern edge of Sgr B2 roughly correlates to the cloud-cloud collision site in Hasegawa et al. (1994). Region N and Region M would be located on the eastern edge of the site while Region U would be located on the western edge. If the active star formation known to occur in Sgr B2 was ignited following the mechanics of the model in Hasegawa et al. (1994), then we would likely expect these three regions to be at the forefront of star forming activity, with the gas in their molecular cores becoming shocked and inducing high star formation. This would allow us to sensibly understand the abundance in star forming characterizations that the line ratios for our star formation tracing molecules exhibit in these regions.

5. CONCLUSION

Using SWAG, we analyzed emission and absorption features towards twelve regions in Sgr B2. We detected 28 of a possible 42 spectral features to be present in these regions throughout the cloud. We were able to characterize physical components of Sgr B2 as well as illustrate the existence of active star forming qualities in three regions in the cloud.

We conclude that the general physical structure of Sgr B2 contains hot, dense molecular cores in the central regions of the cloud, with the outskirts possessing a cooler environment. We also conclude that typical velocities of the gas in the cloud range from ~ 55 km s$^{-1} - \sim 70$ km s^{-1} and that many of the regions possess large velocity widths indicating an ongoing expansion. Furthermore, we found that Region N, Region M, and Region U are chemically rich in star forming features, an illustration that agrees with a possible notion that the active star formation in Sgr B2 was triggered by a cloud-cloud collision near its northwestern edge.

Further work of the project resides in exploring various other regions in Sgr B2, particularly those sources not bright in radio continuum. Additionally, we can study the region indicated by the blue ring in Figure 10 to further understand the star forming features of this area. Work can also be done constraining column densities and star formation rates for the twelve regions analyzed in this report to have further a better understanding of the complexities of Sgr B2, especially the lesser-studied outskirt regions.
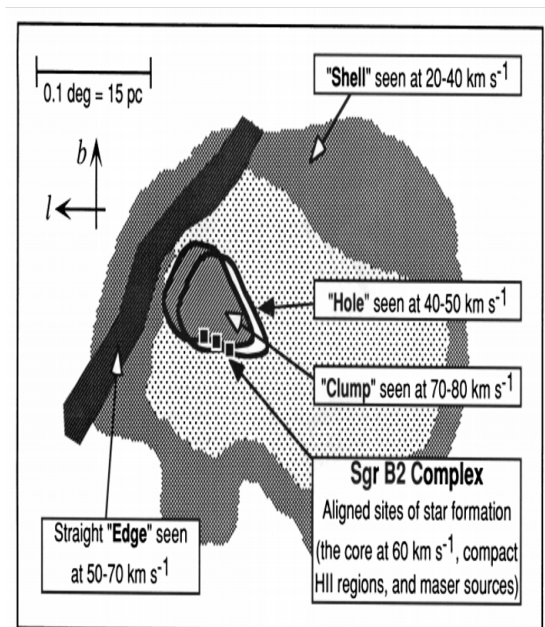

Figure 9. This figure is from Hasegawa et al. (1994) and illustrates the suggested cloud-cloud collision event that triggered high star formation in Sgr B2. The model suggests the Clump collided with a less dense molecular cloud and created the Hole, removing gas with it. The site of this collision is in the northwestern edge of the cloud, matching up with Region N, Region M, and Region U.

We acknowledge support from the National Radio Astronomy Observatory's (NRAO) Research Experience for Undergraduates (REU) program funded by the National Science Foundation (NSF). This project made use of data from the ATCA which we give thanks, as well. The Australia Telescope Compact Array (ATCA) is part of the Australia Telescope National Facility which is funded by the Australian Government for operation as a National Facility managed by the Commonwealth Scientific and Industrial Research Organisation (CSIRO). The National Radio Astronomy Observatory is operated and maintained under a cooperative agreement between Associated Universities, Inc. (AUI) and the National Science Foundation.

Software: CARTA (Comrie et al. 2018), CASA (McMullin et al. 2007), Jupyter (Kluyver et al. 2016), Matplotlib (Hunter 2007), NumPy (Walt et al. 2011), pandas (McKinney et al. 2016), Seaborn (Waskom et al. 2017).
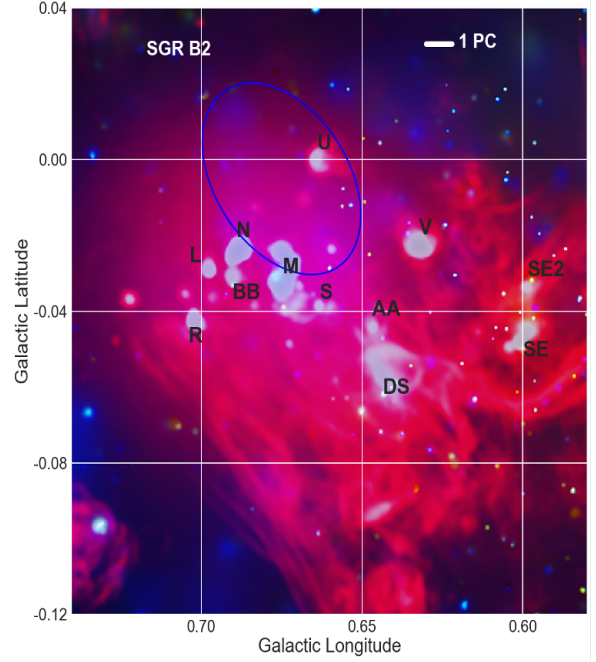
Facilities: ATCA(CABB)

Figure 10. This figure shows a rough location of the cloud-cloud collision event mentioned previously matched with the twelve Sgr B2 regions we analyzed. The region inside the blue ring is the northwestern edge of the cloud, matching up with Region N, Region M, and Region U. Background image credit: (Wang et al. 2019).
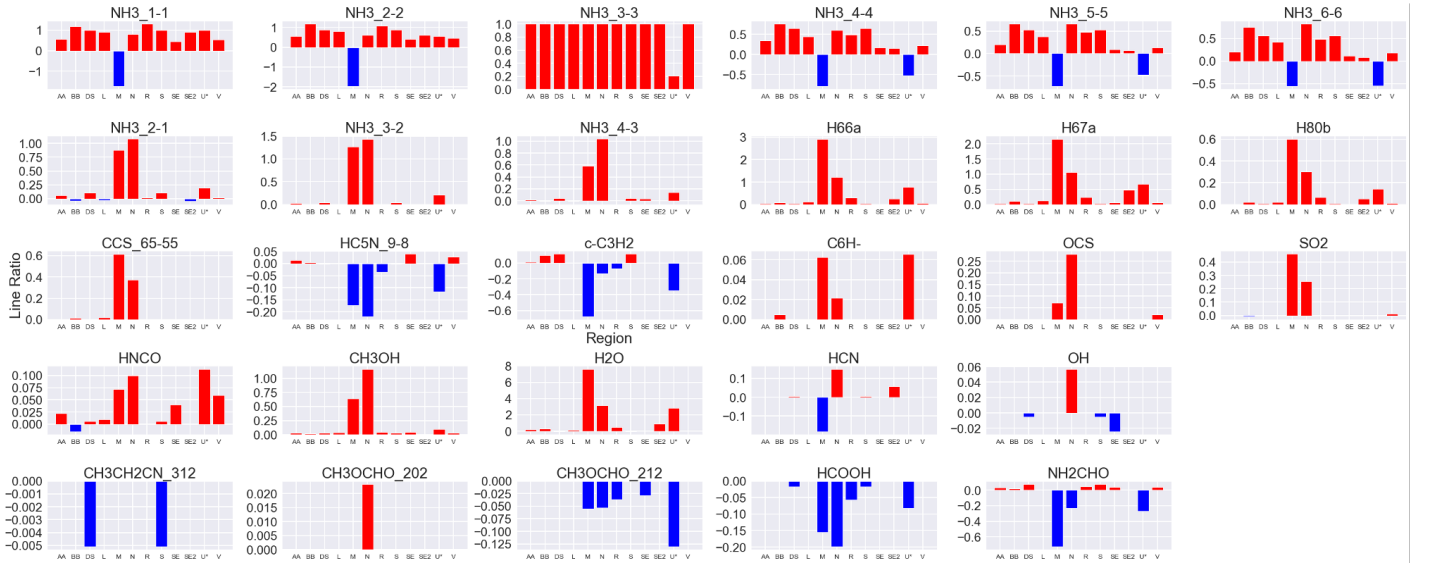
APPENDIX

Figure 11. This figure shows the line ratios for the 28 spectral lines we analyzed in this project. The red bars represent emission components and the blue bars represent absorption components. The blank values correspond to when the emission or absorption component is less than three times the σ value found in Table 4 in Appendix.

Table 4. Summary of Spectral Lines Aimed Toward Sgr B2. Spectral Lines Deleted from Consideration are Noted.

Spectral Line	Transition	Rest Freq. (GHz)	σ (K)	Reason For Deletion
c-C_3H_2	$2_{2,0} - 2_{2,1}$	21.5874	0.043	
C_3H^+	$J = 71/2$, Ω=1/2, $F = 35^+ - 35^-$	22.4898	0.061	Duplicate of HCOOH
$C\alpha$	C64α	24.5221	0.039	Non-detection
$C\alpha$	C66α	22.3753	0.040	Duplicate of H66α
C_6H^-	$8 - 7$	22.0297	0.042	
CCS	$1_2 - 0_1$, $N = 6 - 5$, $J = 5 - 5$	24.5062	0.099	
CH_3C_3N	$6_k - 5_k$	24.7887	0.038	Non-detection
CH_3CH_2CN	$3_{1,2} - 3_{0,3}$, $F = 4 - 4$	24.6585	0.042	
CH_3CH_2CN	$5_{0,5} - 4_{1,4}$	23.7017	0.041	Heavy $NH_3(1,1)$ and $NH_3(2,2)$ contamination
CH_3OCHO	$2_{0,2} - 1_{0,1}$	24.2964	0.037	
CH_3OCHO	$2_{1,2} - 1_{1,1}$	22.8277	0.038	
CH_3OH	$3_{2,1} - 3_{1,2}$	24.9287	0.035	
CH_3OH	$3_{2,1} - 2_{1,3}$	22.9046	0.039	Non-detection
DC_3N	$J = 3 - 2$, $F_1 = 2 - 1$, $F = 1 - 1$	25.3244	0.031	Non-detection
H_2O	$6_{1,6} - 5_{2,3}$, $F = 7 - 6$	22.2350	0.050	
$H\alpha$	H64α	24.5098	0.049	Non-detection
$H\alpha$	H66α	22.3641	0.077	
$H\alpha$	H67α	21.3847	0.042	
$H\beta$	H80β	24.7557	0.031	
HC_5N	$J = 8 - 7$	21.3012	0.039	H96g contamination
HC_5N	$J = 9 - 8$	23.9638	0.025	
HCN	$J = 10 - 10$, $v = 2$	24.6602	0.043	
HCOOH	$1_{0,1} - 0_{0,0}$	22.4711	0.044	
HDO	$5_{3,2} - 5_{3,3}$	22.3076	0.033	Non-detection
$He\alpha$	He66α	22.3732	0.079	H66α contamination
HNCO	$1_{0,1} - 0_{0,0}$, $F = 2 - 1$	21.9814	0.040	
$HOCO^+$	$1_{0,1} - 0_{0,0}$	21.3831	0.051	H67α contamination
NaCN	$6_{1,5} - 6_{1,6}$	23.0052	0.037	Non-detection/possible H87β contamination
NH_2CHO	$1_{0,1} - 0_{0,0}$, $F = 2 - 1$	21.2073	0.055	
$NH_3(1,1)$	$1_10a - 1_10s$, $F_1 = 2-2$, $F = 5/2-5/2$	23.6945	0.051	
$NH_3(2,2)$	$2_20a - 2_20s$, $F_1 = 2 - 2$	23.7226	0.053	
$NH_3(3,3)$	$3_30a - 3_30s$, $F_1 = 2 - 2$	23.8701	0.049	
$NH_3(4,4)$	$4_40a - 4_40s$	24.1394	0.047	
$NH_3(5,5)$	$5_50a - 5_50s$	24.5329	0.042	
$NH_3(6,6)$	$6_60a - 6_60s$	25.0560	0.042	
$NH_3(2,1)$	$2_10a - 2_10s$	23.0988	0.031	
$NH_3(3,2)$	$3_20a - 3_20s$	22.8341	0.034	
$NH_3(4,3)$	$4_30a - 4_30s$	22.6883	0.043	
OCS	$2 - 1$	24.3259	0.045	
OH	$J = 9/2$, $\Omega = 3/2$, $F = 5^- - 5^+$	23.8266	0.037	
SO_2	$8_{1,7} - 7_{2,6}$	25.3927	0.054	
t-C_2H_6O	$2_{2,1} - 3_{1,2}$	22.3672	0.052	Duplicate of H66α

REFERENCES

Comrie, A., Wang, K.-S., Hsu, S.-C., et al. 2018, CARTA: The Cube Analysis and Rendering Tool for Astronomy, Zenodo, doi: 10.5281/zenodo.3377984

Ginsburg, A., et al. 2018, ApJ, 853, 171, doi: 10.3847/1538-4357/aaa6d4

Goldsmith, P. F., Lis, D. C., Hills, R., & Lasenby, J. 1990, ApJ, 350, 186, doi: 10.1086/168372

Hasegawa, T., Sato, F., Whiteoak, J. B., & Miyawaki, R. 1994, ApJ, 429, L77, doi: 10.1086/187417

Henkel, C., Mauersberger, R., Peck, A. B., Falcke, H., & Hagiwara, Y. 2000, AA, 361, L45

Hunter, J. D. 2007, Computing in Science Engineering, 90, doi: 90,doi:10.1109/MCSE.2007.55

Hüttemeister, S., Wilson, T. L., Mauersberger, R., et al. 1995, AA, 294, 667

Kluyver, T., Ragan-Kelley, B., Perez, F., et al. 2016, in ELPUB, 87

Krieger, N., et al. 2017, ApJ, 850, 77, doi: 10.3847/1538-4357/aa951c

Lada, C. J., Forbrich, J., Lombardi, M., & Alves, J. F. 2012, ApJ, 745, 190, doi: 10.1088/0004-637X/745/2/190

Licquia, T. C., & Newman, J. A. 2015, ApJ, 806, 96, doi: 10.1088/0004-637X/806/1/96

Lis, D. C., & Goldsmith, P. F. 1989, ApJ, 337, 704, doi: 10.1086/167141

Longmore, S. N., Bally, J., Testi, L., et al. 2013a, MNRAS, 429, 986, doi: 10.1093/mnras/sts376

Longmore, S. N., Kruijssen, J. M. D., Bally, J., et al. 2013b, MNRAS, 433, L15, doi: 10.1093/mnrasl/slt048

McKinney, W., et al. 2016, in Proceedings of the 9th Python in Science Conference, 51

McMullin, J. P., Waters, B., Schiebel, D., Young, W., & K, G. 2007, Astronomical Data Analysis Software and Systems XVI (ASP Conf. Ser. 376), ed. R. A. Shaw, F. Hill, D. J. Bell (San Francisco, CA: ASP), 127

Mehringer, D. M., Palmer, P., Goss, W. M., & Yusef-Zadeh, F. 1993, ApJ, 412, 684, doi: 10.1086/172954

Pree, C. G. D., Goss, W. M., & Gaume, R. A. 1998, ApJ, 500, 847, doi: 10.1086/305782

Walmsley, C. M., & Ungerechts, H. 1983, AA, 122, 164

Walt, S. V. D., Colbert, S. C., & Varoquaux, G. 2011, Computing in Science Engineering, 22

Wang, D., et al. 2019, X-ray and Radio Images of the Galactic Center

Waskom, M., Botvinnik, O., O'Kane, D., et al. 2017, doi: doi:10.5281/zenodo.883859

Zeng, S., Zhang, Q., Jiménez-Serra, I., et al. 2020, Monthly Notices of the Royal Astronomical Society, 497, 4896–4909, doi: 10.1093/mnras/staa2187